

## Article

# $^6\text{LiF}$ Converters for Neutron Detection: Production Procedures and Detector Tests

Antonio Massara <sup>1</sup>, Simone Amaducci <sup>1</sup>, Luigi Cosentino <sup>1</sup>, Fabio Longhitano <sup>2</sup>, Carmelo Marchetta <sup>1,†</sup>, Gaetano Elio Poma <sup>1</sup>, Martina Ursino <sup>1</sup> and Paolo Finocchiaro <sup>1,\*</sup>

<sup>1</sup> INFN Laboratori Nazionali del Sud, 95123 Catania, Italy

<sup>2</sup> INFN Sezione di Catania, 95123 Catania, Italy

\* Correspondence: finocchiaro@lns.infn.it

† Now retired.

**Abstract:** Several methods to detect thermal neutrons make use of the naturally occurring  $^6\text{Li}$  isotope, as it has a rather high cross-section for neutron capture followed by a decay into an alpha particle and a triton. Due to the high chemical reactivity of lithium, the use of the stable isotopic salt  $^6\text{LiF}$  is generally preferred to the pure  $^6\text{Li}$ . The typical method for depositing thin layers of  $^6\text{LiF}$  on suitable substrates, therefore creating so-called neutron converters, is evaporation under vacuum. The evaporation technique, as well as a newly developed chemical deposition process, are described along with their benefits and drawbacks, and the results of neutron detection tests performed with the two types of converters coupled to silicon diodes show convenient performances.

**Keywords:** neutron converter; lithium fluoride; neutron detection



**Citation:** Massara, A.; Amaducci, S.; Cosentino, L.; Longhitano, F.; Marchetta, C.; Poma, G.E.; Ursino, M.; Finocchiaro, P.  $^6\text{LiF}$  Converters for Neutron Detection: Production Procedures and Detector Tests. *Instruments* **2023**, *7*, 1. <https://doi.org/10.3390/instruments7010001>

Academic Editors: Antonio Ereditato and Pasquale Arpaia

Received: 29 November 2022

Revised: 19 December 2022

Accepted: 20 December 2022

Published: 23 December 2022



**Copyright:** © 2022 by the authors. Licensee MDPI, Basel, Switzerland. This article is an open access article distributed under the terms and conditions of the Creative Commons Attribution (CC BY) license (<https://creativecommons.org/licenses/by/4.0/>).

## 1. Introduction

Neutron detection plays an important role in several fields, not only in physics research but also in nuclear engineering, material science, radioactive waste management, homeland security, and nuclear medicine [1–5]. As the neutron is an electrically neutral particle, its detection requires indirect detection methods that make use of a so-called neutron converter, i.e., a nuclear species featuring a conveniently large neutron absorption cross-section and a decay channel involving charged particles. By detecting (one or more) such outgoing charged particles, one can infer the detection of a neutron. High energy neutrons can be detected by exploiting their elastic scattering on hydrogen and detecting the outgoing proton. The detection of thermal neutrons (i.e., with 0.025 eV kinetic energy corresponding to  $\approx 290^\circ\text{K}$ ) is much easier, as the neutron absorption cross-section at low energy is basically proportional to the inverse of the neutron velocity in most elements. Therefore, one can make use of neutron moderators, i.e., bulk materials containing light nuclear species, which are quite efficient in slowing neutrons down to thermal energy with few elastic collisions. The widely used moderator material is polyethylene, which consists of carbon and hydrogen atoms.

The most convenient neutron converter species are  $^3\text{He}$ ,  $^{10}\text{B}$ , and  $^6\text{Li}$ , according to the reactions listed in Table 1 along with their respective cross-sections. The most widely employed neutron detectors so far have been based on  $^3\text{He}$ , due to its large reaction cross-section and excellent insensitivity to background gamma radiation. During the last decade, a considerably reduced availability of  $^3\text{He}$  [6], with the consequent price increase, has triggered a worldwide R&D program focused on the development of new neutron detection techniques [7–9].

**Table 1.** Useful neutron conversion reactions and their respective thermal cross-sections.

Reaction	Cross-Section [b]
$n + {}^3\text{He} \rightarrow {}^3\text{H} + p + \gamma$	5333
$n + {}^{10}\text{B} \rightarrow {}^7\text{Li} + {}^4\text{He} + \gamma$	3607
$n + {}^{10}\text{B} \rightarrow {}^7\text{Li} + {}^4\text{He}$	230
$n + {}^6\text{Li} \rightarrow {}^3\text{H} + {}^4\text{He}$	940

The choice of converter material is generally bound to the specific application. In particular, if planning to use a solid-state detector, a reaction lacking  $\gamma$ -rays is preferred in order to strongly reduce the background noise due to gamma ray signals being wrongly interpreted as neutron detection. This is why, when using a semiconductor detector for secondary particles following neutron capture, the preferred converter is  ${}^6\text{Li}$  [10–20]. However, due to the high chemical reactivity of lithium, the use of the stable isotopic salt  ${}^6\text{LiF}$  is generally preferred to pure  ${}^6\text{Li}$ .

The thermal neutron capture reaction of  ${}^6\text{Li}$  produces an alpha particle and a triton, emitted back-to-back with kinetic energies of 2.05 and 2.73 MeV, respectively. Either of the two particles can be detected after losing some of its energy while moving through the converter before reaching the detector. The amount of loss depends on the interaction depth, converter material, particle type, and initial energy. Moreover, the particle entering the detector must have sufficient residual energy in order to produce a signal large enough to be discriminated from the gamma (or noise) background. The range of the two particles in  ${}^6\text{LiF}$  is about 6.5  $\mu\text{m}$  for alphas and 22  $\mu\text{m}$  for tritons. As a consequence, the choice of film thickness that can be practically used is limited, and for a  ${}^6\text{LiF}$  converter coupled to a silicon diode, the maximum useful thickness is around 16  $\mu\text{m}$ , above which the detection efficiency saturates [17].

The usual method for depositing thin layers of  ${}^6\text{LiF}$  on suitable substrates is evaporation under vacuum. One of the practical applications of detectors employing evaporated  ${}^6\text{LiF}$  converters is the monitoring of neutron radiation from radioactive waste drums. This goal was pursued within the framework of the H2020 EURATOM project MICADO [20,21] by installing a few detectors around each drum. These detectors, called SiLiF, employ double-sided  $3 \times 3 \text{ cm}^2$  silicon diodes and  ${}^6\text{LiF}$  converters enclosed in  $10 \times 10 \times 10 \text{ cm}^3$  polyethylene moderators.

Within the framework of the H2020 EURATOM project CLEANDEM [22], an unmanned ground vehicle (UGV) is being developed for nuclear decommissioning and/or remediation, and a miniaturized neutron counter is required onboard the UGV for a fast dose rate map acquisition. This detector, called miniSiLiF, consists of a  $1 \times 1 \text{ cm}^2$  silicon diode coupled to a  ${}^6\text{LiF}$  layer. In order to minimize the waste of the isotopically enriched  ${}^6\text{LiF}$ , unavoidable with such a small size in the evaporation technique, a chemical deposition technique was developed that makes possible the production of single converters.

In the following, the evaporation technique and the newly developed chemical deposition process will be described, along with their benefits and drawbacks, and the results of neutron detection tests performed with the two types of converters in the SiLiF and miniSiLiF configurations will be shown.

## 2. The Evaporation Technique

### 2.1. Converter Production with the Smaller Evaporator

The physical vapor deposition technique (PVD), so far employed in our previous research and development activity, is still currently used to deposit layers of the isotopic  ${}^6\text{LiF}$  salt on suitable substrates. The salt, enriched at 95% in  ${}^6\text{Li}$ , was provided by Sigma Aldrich [23]. Several different substrates were tested, namely mylar and kapton down to 2  $\mu\text{m}$  thickness, and aluminum, glass, silicon, and carbon fiber in the 0.1–2 mm thickness range; they all showed quite good adhesion properties. The salt to be evaporated is

placed inside a vacuum chamber on a small molybdenum crucible kept in place by two water-cooled electrodes. A suitable electrical current heats the crucible and the salt, which evaporates (Figure 1) and diffuses through the chamber, reaching the substrates and condensing on their surface. The substrates have to be placed at a convenient distance in order to minimize geometrical nonuniformities due to their proximity to the crucible. The first prototype converters were produced in a small evaporator employing a Pyrex glass cylinder inside a vacuum chamber 30 cm in diameter, as shown in Figure 2. The cylinder reduces the waste of material that otherwise would be deposited on the chamber walls and need to be cleaned at the end of the production procedure. The prototypes had an area of  $5 \times 5 \text{ cm}^2$  and could only be produced in batches of four, due to the limited size of the evaporation chamber.

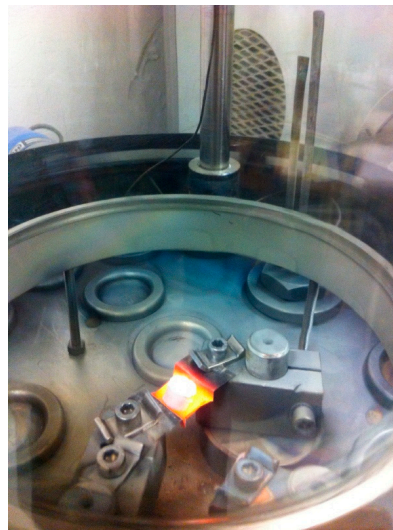


**Figure 1.**  $^6\text{LiF}$  being evaporated under vacuum from a hot crucible.

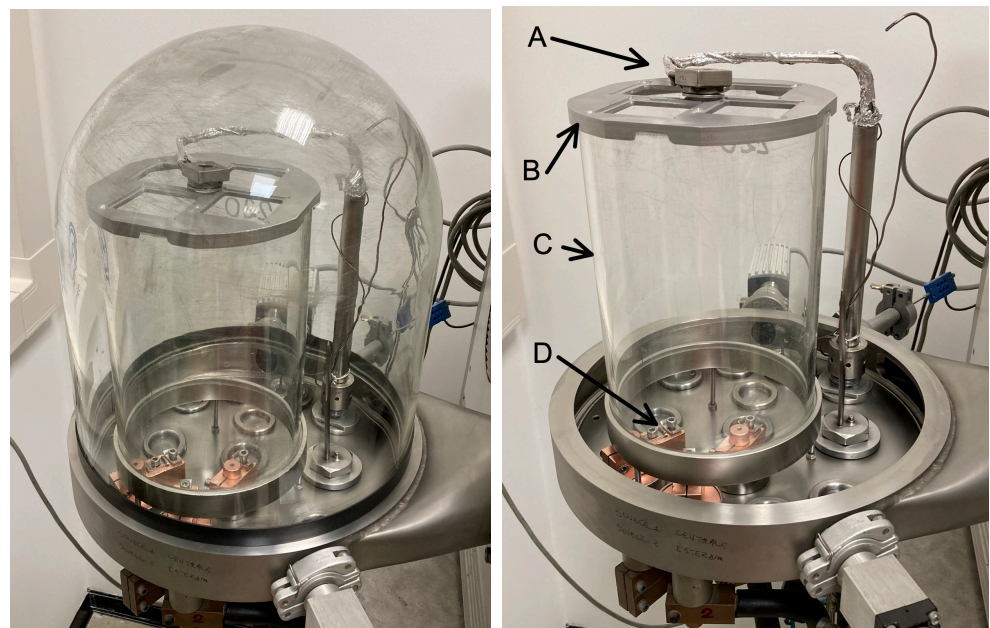


**Figure 2.** The small evaporator with the Pyrex glass vacuum chamber 30 cm in diameter. (A): quartz scale. (B): support for substrates. (C): Pyrex glass cylinder to limit the evaporation spread. (D): electrodes/holders for the crucible.

A picture of the mechanical support for the substrates is shown in Figure 3. A quartz oscillator, to be installed during evaporation in correspondence with the middle round hole, acts as a scale to weigh the amount of evaporated salt. Indeed, while the hot pellet evaporates, a thin film is deposited also onto the oscillator, thus increasing the oscillating mass and making the oscillation frequency decrease correspondingly. By measuring such a decrease, one can deduce the deposited layer thickness and stop the process when the programmed value is reached.

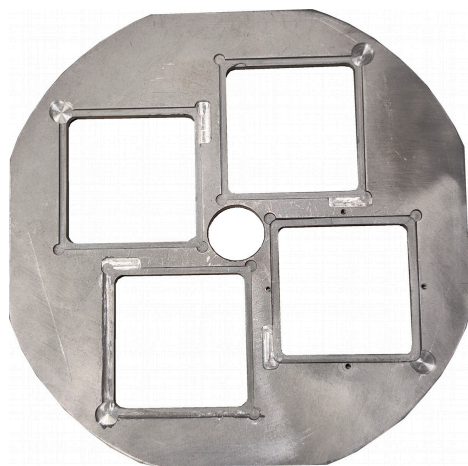


**Figure 3.** Mechanical support for the substrates.

The effectiveness of this method was cross-checked by depositing a thin layer of  ${}^6\text{LiF}$  ( $1.8\ \mu\text{m}$  at nominal density, i.e.,  $458\ \mu\text{g}/\text{cm}^2$ ) onto thicker aluminum foil ( $6\ \mu\text{m}$  as indicated on the manufacturer datasheet) and measuring the thicknesses by means of the energy lost by alpha particles when crossing the layers. This method can only be exploited with thin layers of converter and substrate, as the alpha particles have to cross them and reach a silicon detector suitably placed behind the sample. The measurement was done in three steps inside a vacuum chamber: (A) a Pu-Am-Cm alpha source was placed in front of the silicon detector with a collimator in between; (B) the aluminum foil was placed in front of the detector; (C) the aluminum foil with the evaporated  ${}^6\text{LiF}$  layer was placed in front of the detector (Figure 4).

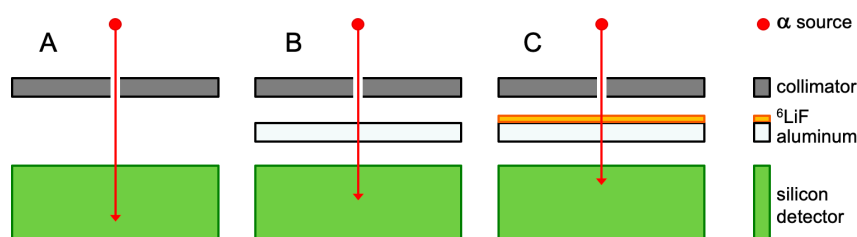


**Figure 4.** Sketch of the three steps of the measurement of the thickness of the thin layers using an alpha source and a silicon diode.

The recorded spectra in the three configurations show peaks at 5.148, 5.477, and 5.794 MeV from  ${}^{239}\text{Pu}$ ,  ${}^{241}\text{Am}$ , and  ${}^{244}\text{Cm}$ , respectively, clearly degraded by the crossed material thickness in B and C (Figure 5). The detector was calibrated in energy in configuration A, then the centroid of each peak in configuration B and C was used to calculate the energy losses for three categories of alpha particles as the distance between each pair of corresponding centroids. Knowing the initial energy, the energy loss ( $E_{\text{loss}}$ ), and the crossed material, one can infer the thickness by using a tool based on the Bethe and Bloch formula [24]. In order to show more directly understandable numbers, we prefer to report thickness in micrometers instead of areal density, assuming the standard density values for



each material. The resulting thicknesses are listed in Table 2 along with the corresponding nominal values. The nominal thickness set by means of the quartz oscillator was found to underestimate the measured thickness, while the uncertainty introduced by the energy loss method is basically negligible.

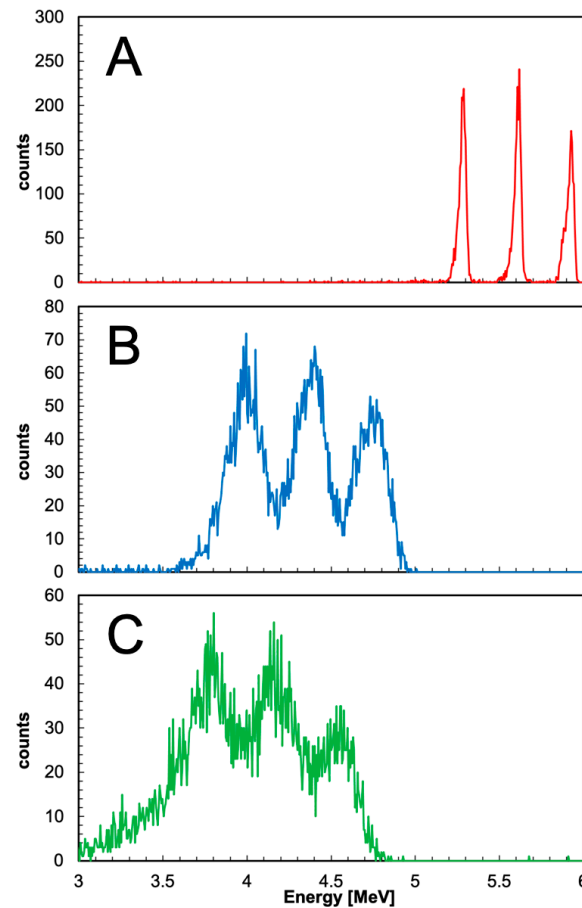


**Figure 5.** The alpha particle energy spectra recorded at each thickness measurement step. (A) no material between source and detector. (B) aluminum layer (6  $\mu\text{m}$  nominal) between source and detector. (C)  $^6\text{LiF}$  and aluminum layers (1.8  $\mu\text{m}$  and 6  $\mu\text{m}$  nominal, respectively). See also Table 1.

**Table 2.** The nominal and measured thickness of the aluminum and  $^6\text{LiF}$  layers, assuming standard densities. The quoted systematic uncertainty due to the energy loss method employed is basically negligible.

Layer Material	Nominal Thickness [ $\mu\text{m}$ ]	Measured Thickness [ $\mu\text{m}$ ]	Systematic Uncertainty $E_{\text{loss}}$ Method [ $\mu\text{m}$ ]
Aluminum	6	6.3	0.018
$^6\text{LiF}$	1.8	1.9	0.005

In light of these results, a series of measurements was performed on three different thin converters denoted as LiF-01, LiF-02, and LiF-03 and belonging to the same evaporated batch. Their thickness was measured at three or five positions according to the scheme shown in Figure 6 in order to evaluate the uniformity of the evaporated layers. The measured thicknesses are reported in Figure 7, where one can immediately see that the maximum observed nonuniformity is on the order of a few nanometers, and thus negligible. The plot in Figure 8 shows the percent deviation of each measured thickness from the average value, with the vertical dashed line indicating the nominal value set by means of the quartz oscillator. The three converters were successfully tested by placing them on

top of a  $3 \times 3 \text{ cm}^2$  silicon detector exposed to a thermalized AmBe neutron source that produces  $2.2 \times 10^6$  neutrons/s, with a flux of about 2000 thermal neutrons/s/cm<sup>2</sup> in the measurement position. As an example, the obtained deposited energy spectrum of Figure 9 for the LiF01 sample shows the contributions of tritons, alphas, and background gamma rays [8]. While the hardware threshold around 0.4 MeV suppressed any electrical noise, a suitable software threshold around 1.8 MeV allows one to select only tritons as a signature of neutron detection.

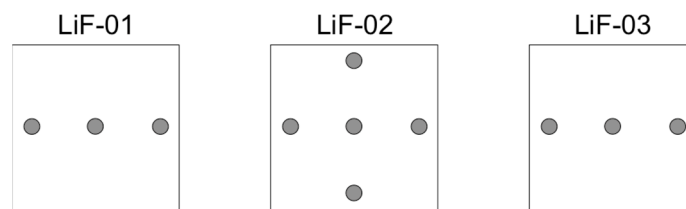


**Figure 6.** Scheme of the thickness measurement positions of the three thin samples. The nominal thickness was  $1.8 \text{ }\mu\text{m}$  ( $^6\text{LiF}$ ) and  $6 \text{ }\mu\text{m}$  (aluminum substrate).

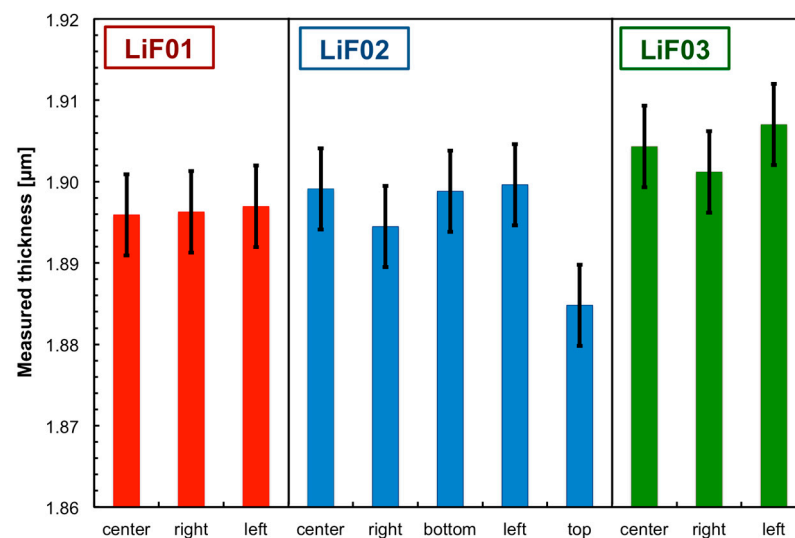


**Figure 7.**  $^6\text{LiF}$  thickness measured for the three thin samples in the positions indicated by Figure 6. The nominal value was  $1.8 \text{ }\mu\text{m}$ .

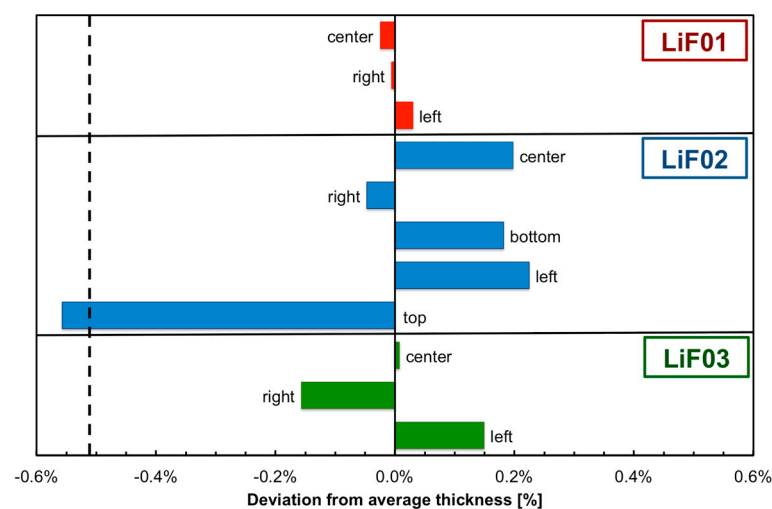


**Figure 8.** Deviation from the average  $^6\text{LiF}$  thickness of the three thin samples. The vertical dashed line refers to the nominal value ( $1.8 \text{ }\mu\text{m}$ ) set by means of the quartz oscillator.

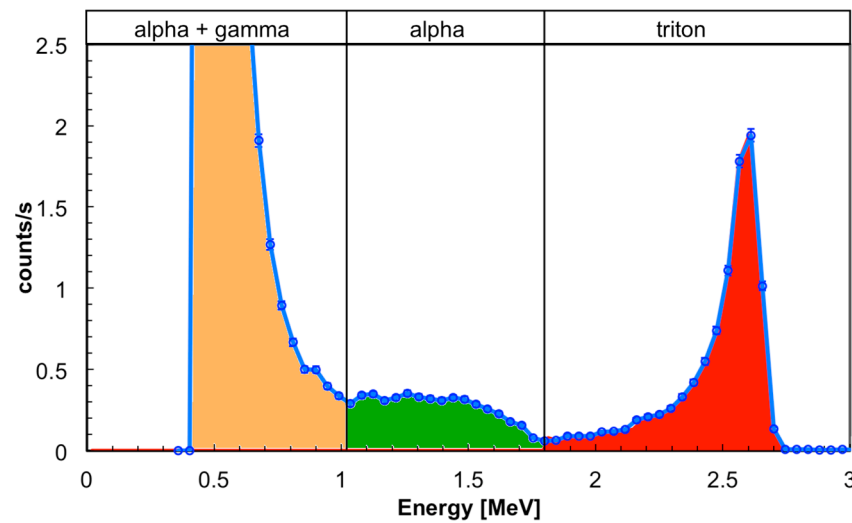


**Figure 9.** Deposited energy spectrum measured from the LiF01 sample (1.8  $\mu\text{m}$  nominal thickness) placed on a  $3 \times 3 \text{ cm}^2$  silicon detector exposed to a thermalized AmBe neutron source.

## 2.2. Converter Production with the Larger Evaporator

The MICADO project was required to produce 74 converters with 16  $\mu\text{m}$  nominal thickness on  $50 \times 50 \times 1 \text{ mm}^3$  carbon fiber substrates, and this required employment of a bigger evaporator with a 50 cm diameter vacuum chamber. The evaporator and the mechanical support that can host 22 substrates are shown in Figure 10. The support was installed on a rotating carousel in order to obtain a uniform deposition across all the converters.

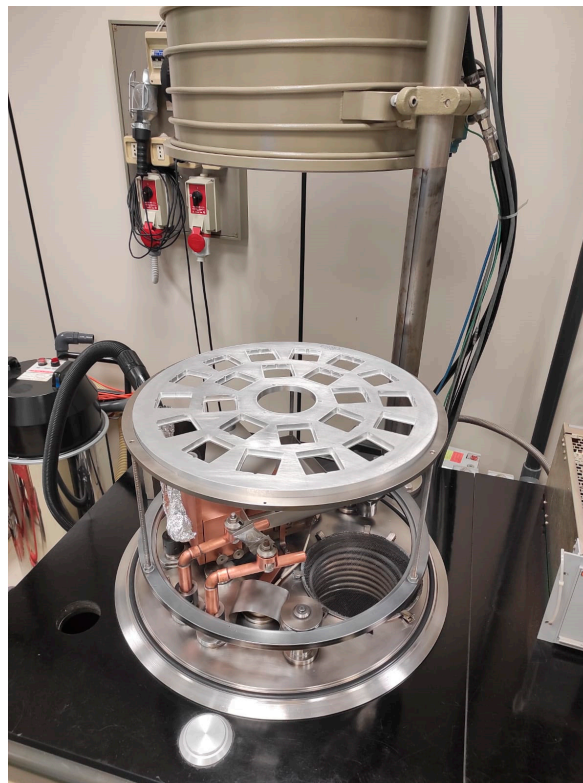


**Figure 10.** The 50 cm diameter evaporator with support for 22 substrates.

The production of the 74 samples was done in four batches. Even though the quartz scale method is reasonably reliable, the amount of  $^6\text{LiF}$  actually deposited was cross-

checked on a selected number of samples. Eight samples from positions 1, 3, 5, 7, 9, 13, 16, and 20, were selected from runs 1–3, and only four from positions 1, 3, 5, and 7 from run 4, according to the scheme in Figure 11. Each sample was weighed before and after evaporation using a 10 µg precision scale, thus obtaining the amount of deposited  $^6\text{LiF}$  that, divided by the effective area, provided the areal density. The nominal required value for the areal density was  $4068 \mu\text{g}/\text{cm}^2$ , corresponding to  $16 \mu\text{m}$  of  $^6\text{LiF}$  at standard density. As could be expected from the considerations in the previous section, the nominal thickness set by means of the quartz oscillator underestimated the effective measured thickness. Indeed, the average thickness came out as  $16.87 \pm 0.37 \mu\text{m}$ , corresponding to an areal density of  $4290 \pm 94 \mu\text{g}/\text{cm}^2$ .

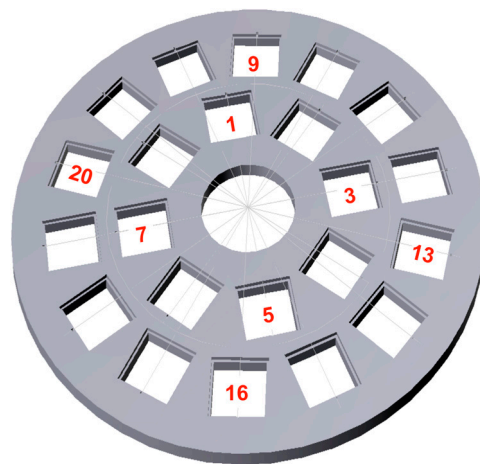


**Figure 11.** Scheme of the samples selected for the weight analysis.

The measured thicknesses are reported in Figure 12, whereas the plot in Figure 13 shows the deviation of the measured thicknesses from the average value for the 28 converters tested. No particular correlation was observed with the position of the samples on the carousel.

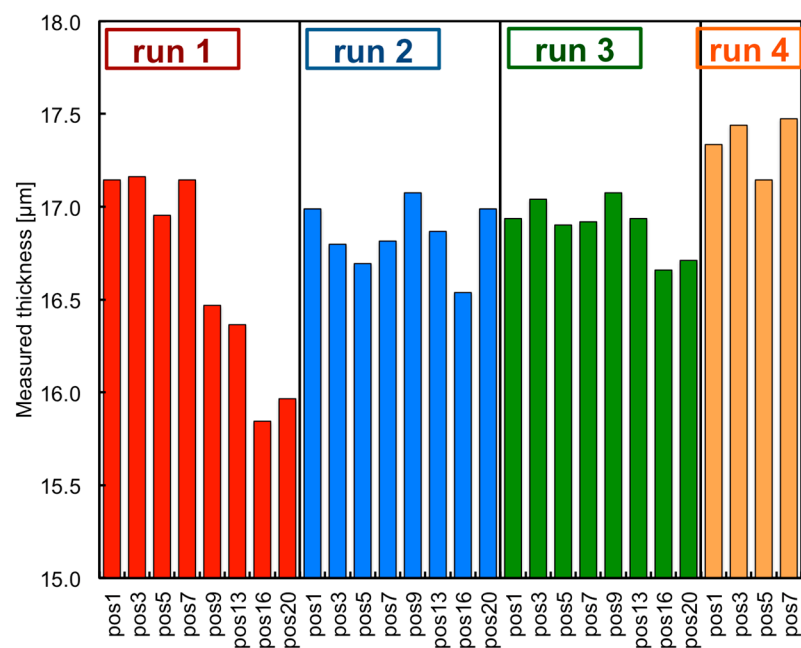


**Figure 12.** The measured thicknesses for the 28 samples.



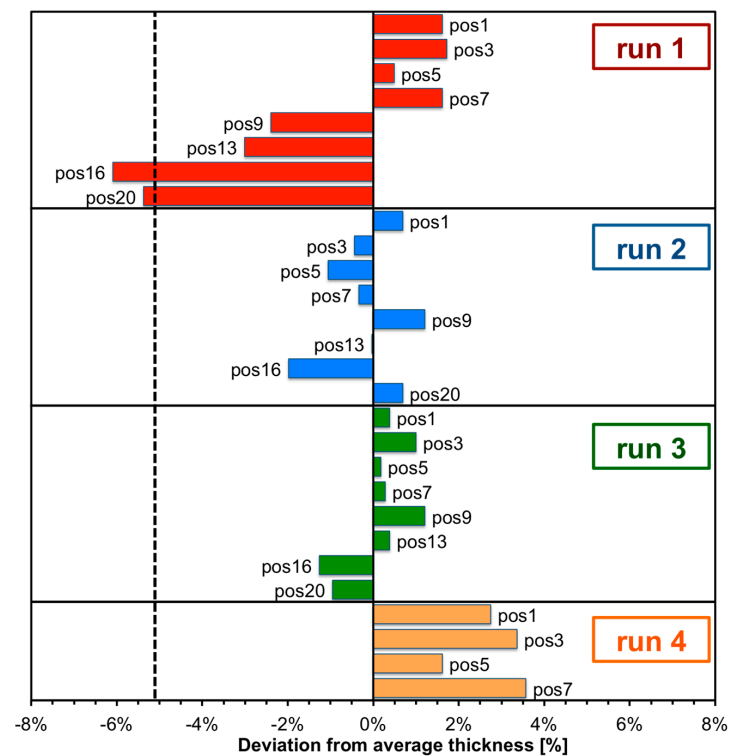


**Figure 13.** The deviation from the average thickness for the 28 samples. The vertical dashed line indicates the nominal value set by means of the quartz oscillator.

Each converter was successfully assembled on top of a  $3 \times 3 \text{ cm}^2$  silicon detector and exposed to a thermalized AmBe neutron source. As an example, the obtained deposited energy spectrum of Figure 14 for one of the produced detectors shows the contributions of tritons plus alphas and alphas plus background gamma rays. This plot differs from Figure 9 because of the larger thickness of the converter. The contribution of tritons and alphas spreads toward low energy due to the increasing energy loss for particles produced more deeply in the  $^6\text{LiF}$  layer. Additionally, in this case, the hardware threshold suppressed any electrical noise. The safe software threshold to suppress the gamma ray contribution was chosen as 1.5 MeV, with alpha and triton separation no longer visible [20].

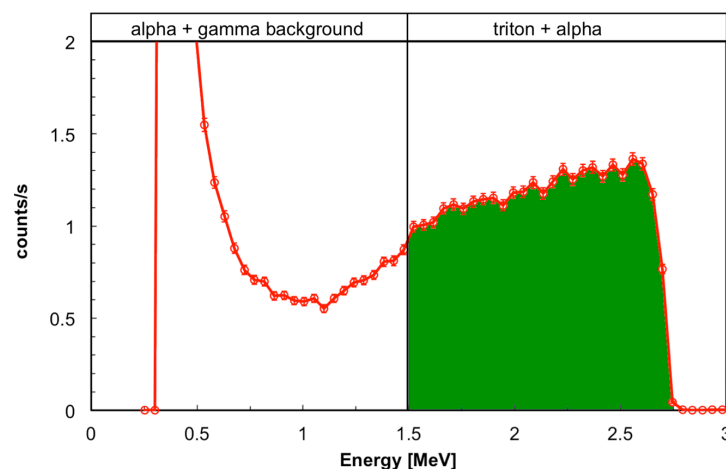
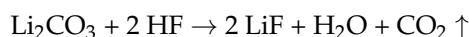


**Figure 14.** Deposited energy spectrum measured with one of the samples placed on a  $3 \times 3 \text{ cm}^2$  silicon detector exposed to a thermalized AmBe neutron source.

### 3. The Chemical Deposition Technique

The required deposition of  ${}^6\text{LiF}$  converters on substrates with much smaller areas, as foreseen in the CLEANDEM project, posed the problem of quick production of few samples with a reduced effort in terms of equipment and manpower. A solution was searched for and found in a chemical deposition technique.

The lithium fluoride salt is scarcely soluble in water, with a value of  $K_{ps} = 1.84 \times 10^{-3}$  at 25 °C, corresponding to a solubility of 1.11 g/l (1.08 g/l for  ${}^6\text{LiF}$  enriched at 95%). Starting from lithium carbonate and hydrofluoric acid, the following reaction was exploited to produce lithium fluoride and gaseous carbon dioxide.



A dedicated mini-well support made of polyethylene was designed, resistant to hydrofluoric acid, that is closed at the bottom by the converter substrate. The required amount of  ${}^6\text{Li}_2\text{CO}_3$  was spread onto the substrate inside the mini-well, and the setup was placed under a chemical fume hood. Then, a suitable amount of HF solution was poured in, along with a few microliters of demineralized water to improve the uniform distribution of the salt, and the reaction started with visual feedback provided by  $\text{CO}_2$  bubbling up from the solution. The setup was kept under the hood until water was visible, with the  ${}^6\text{LiF}$  salt deposit left on the bottom. In order to remove the residual humidity, it was placed in an oven under vacuum at 105 °C for twelve hours, and then it was left to cool down to ambient temperature still in vacuum. The pictorial scheme in Figure 15 summarizes the above-described phases of the chemical deposition procedure up to the detector assembly and neutron detection. The pictures in Figure 16 display the assembly of a carbon fiber substrate on the bottom of the mini-well and the setup at the end of the deposition.

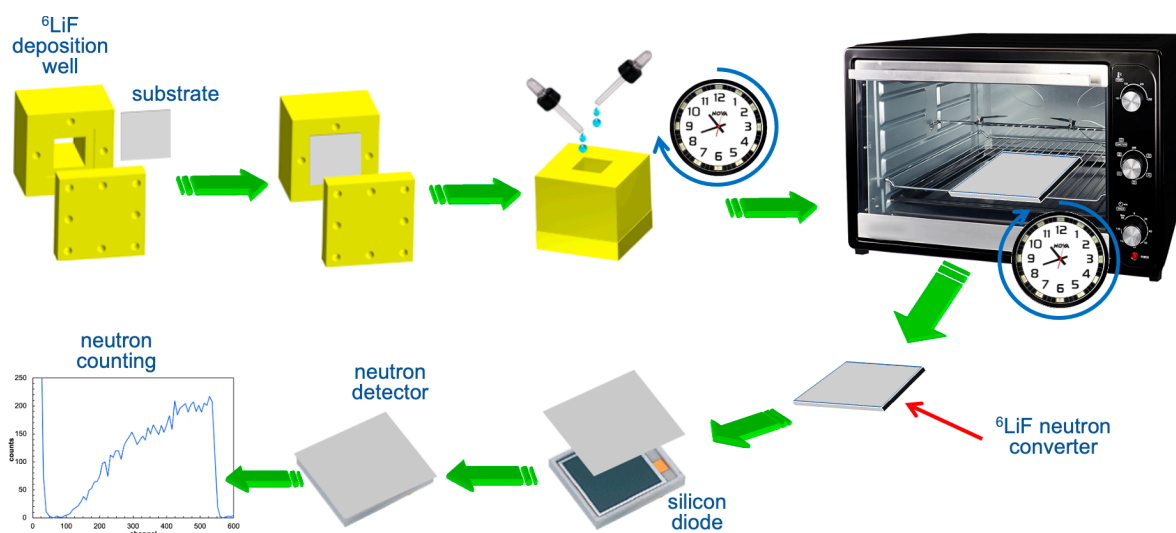


**Figure 15.** Pictorial scheme summarizing the phases of the chemical deposition technique for the production of a  ${}^6\text{LiF}$  neutron converter layer onto a suitable substrate.

Unfortunately, this procedure produces a salt layer that does not adhere strongly enough to the substrate, as immediately evident from the visual appearance of the deposited layer. Indeed, the surface is also grainy; thus, its uniformity is far from what was obtained with the evaporation technique described before. Nonetheless, apart from high-precision applications where the uniformity may be important for reproducible detection efficiency, in several cases it is not so relevant. The main issue that remained was preventing the loss of salt from the surface when brushing even lightly against the converter or simply moving it. This was solved by coating the converter with a thin (a few nanometers in scale) layer of a resistant and transparent polymeric thermoplastic resin called Formvar. This was

achieved by briefly immersing it into a suitable solution and then letting it dry. A number of tests made it possible to calibrate the quantities of each reagent required to obtain a given final amount of  $^6\text{LiF}$  on the substrate that can be checked by weighing the samples before and after deposition on a high-precision scale.

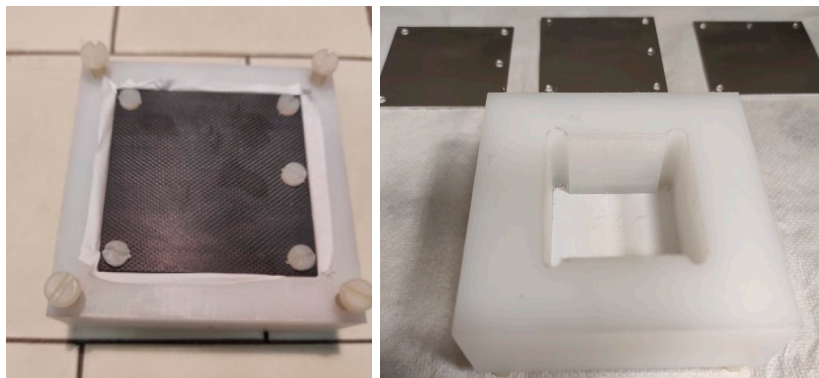


**Figure 16.** (Left): the mini-well assembly with a carbon fiber substrate on the bottom. (Right): the setup at the end of the deposition.

In Figure 17, a comparison is shown between two spectra obtained with a converter chemically deposited and a reference evaporated one. In both cases, the nominal thickness at standard density was  $16\text{ }\mu\text{m}$ , and the converters were coupled to identical  $3 \times 3\text{ cm}^2$  silicon detectors. The two detectors were placed in turn in the same position facing a thermalized AmBe neutron source. The plot shows that, for this thickness, the behavior is identical regardless of the possible different uniformity. It should be remarked that  $16\text{--}17\text{ }\mu\text{m}$  is the thickness after which the detection efficiency saturates [17].

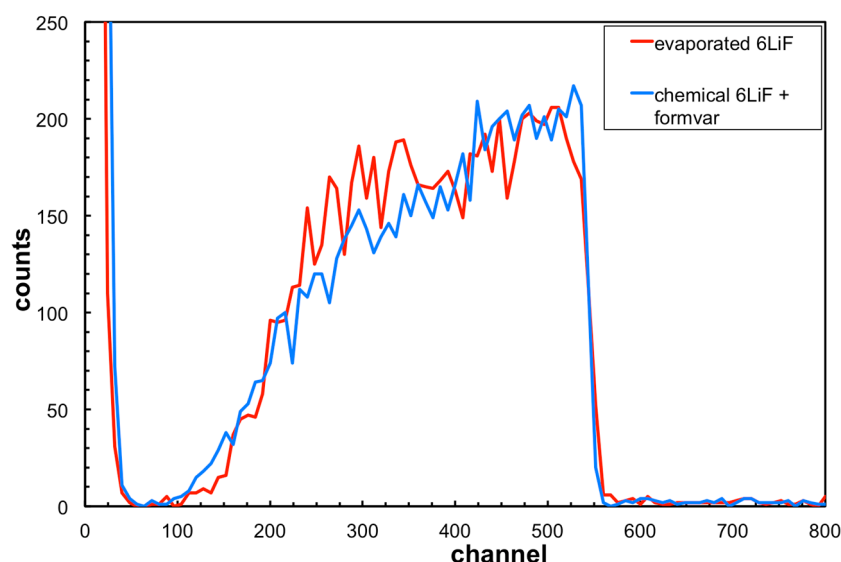


**Figure 17.** Comparison between two spectra obtained with a converter chemically deposited and a reference evaporated one. The nominal converter thickness was  $16\text{ }\mu\text{m}$ .

#### 4. Discussion

The three methods of  $^6\text{LiF}$  layer production can coexist, and each time, one has to choose the most appropriate method according to several factors.

The smaller evaporator, which also exploits a Pyrex glass cylinder to confine the evaporation plume, is well-suited for the production of a restricted number of samples. It involves relevant waste material that in the end is left on the walls of the cylinder itself, on the circular support of the samples, and on the bottom of the chamber. The maximum

rectangular sample area that can be arranged on a suitably designed support is on the order of  $10 \times 5 \text{ cm}^2$ . The benefit of the smaller evaporator is the optimal uniformity of the deposition, especially when producing micron or submicron thickness layers.

The larger evaporator has to be involved when producing a relevant number of samples. It also allows for the production of wide-area rectangular samples, roughly up to  $30 \times 20 \text{ cm}^2$ . The price to pay is a slightly worse thickness uniformity across the samples, even in the same batch, and a much higher amount of material waste. Indeed, for the production of the 74 samples described above, the useful amount of  $^6\text{LiF}$  was about 7 g in light of the total 60 g required to perform the process. Moreover, in order to reach the desired thickness, 15 loads of  $^6\text{LiF}$  on the crucible were necessary, and therefore 15 runs for a total duration of several days.

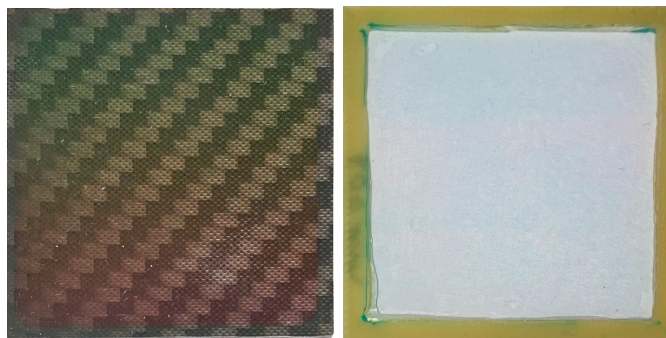
The chemical deposition technique, better suited for the quick production of single converters, produces lower quality, grainy, and rough samples, lacking good uniformity and reproducibility. As long as one needs only an average amount of  $^6\text{LiF}$  on the substrate and does not care much about a precise a priori determination of the neutron detection efficiency, this type of converter is much cheaper, as it does not need the complex and expensive evaporator equipment, is faster, and requires a considerably lower amount of manpower.

A summary comparing the main features for the three production methods of  $^6\text{LiF}$  layers is reported on Table 3.

**Table 3.** Comparison of the main features for the three  $^6\text{LiF}$  deposition methods.

	Small Evaporator	Large Evaporator	Chemical Process
<b>n. samples</b>	$\approx 4$ units	$\approx 22$ units	single
<b>material waste ratio</b>	$\approx 5:1$	$\approx 8.5:1$	$\approx$ negligible
<b>max sample area</b>	$\approx 10 \times 5 \text{ cm}^2$	$\approx 30 \times 20 \text{ cm}^2$	depends on the well size
<b>thickness uniformity</b>	very good ( $\approx 0.2\%$ )	good ( $\approx 2\%$ )	rough (not measured)
<b>best suited for</b>	micron or submicron thickness	10–20 $\mu\text{m}$ thickness	10–20 $\mu\text{m}$ , not for well-calibrated efficiency detectors
<b>equipment complexity and cost</b>	medium	high	low

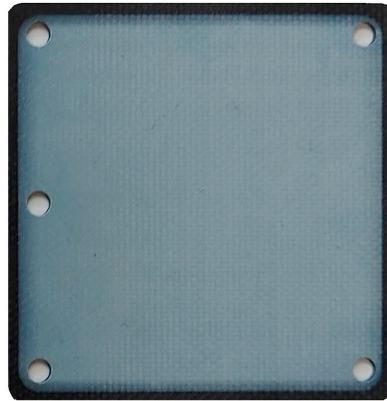
Figure 18 shows two  $5 \times 5 \text{ cm}^2$  converters produced with the smaller evaporator, respectively, 40 nm ( $10 \mu\text{g}/\text{cm}^2$ ) on 0.6 mm thick carbon fiber and 1.6  $\mu\text{m}$  ( $400 \mu\text{g}/\text{cm}^2$ ) on 2  $\mu\text{m}$  mylar. The latter was tightly glued on a resin frame to keep it flat. The lefthand picture has some slight multicolor nuances produced by chromatic interference due to the ultra-thin deposited layer.



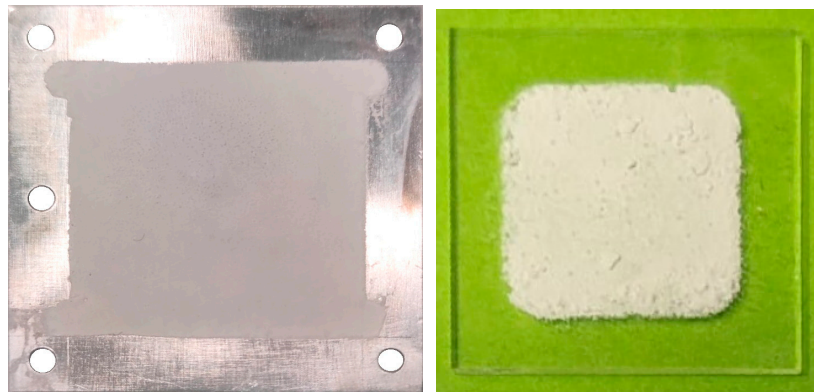
**Figure 18.** Two  $5 \times 5 \text{ cm}^2$   $^6\text{LiF}$  converters produced with the smaller evaporator. (Left): 40 nm ( $10 \mu\text{g}/\text{cm}^2$ ) on 0.6 mm carbon fiber. (Right): 1.6  $\mu\text{m}$  ( $400 \mu\text{g}/\text{cm}^2$ ) on 2  $\mu\text{m}$  mylar.



Figure 19 shows one of the 74 converters ( $16\ \mu\text{m}$  nominal layer thickness) deposited on a 1 mm thick carbon fiber substrate by means of the larger evaporator. Finally, in Figure 20, two converters ( $16\ \mu\text{m}$  nominal layer thickness) produced by means of the chemical deposition technique are shown. The lefthand one was deposited on a  $5 \times 5\ \text{cm}^2$  aluminum substrate using a larger mini-well. The righthand one was deposited on a  $2 \times 2\ \text{cm}^2$  glass substrate using a smaller mini-well. Notice that the two pictures are not to scale.



**Figure 19.** One of the 74  $^{6}\text{LiF}$  converters ( $16\ \mu\text{m}$  nominal layer thickness) deposited on a 1 mm thick carbon fiber substrate by means of the larger evaporator.



**Figure 20.** Two converters,  $16\ \mu\text{m}$  nominal layer thickness, produced by means of the chemical deposition technique. **(Left):** on a  $5 \times 5\ \text{cm}^2$  aluminum substrate, using a larger mini-well. **(Right):** on a  $2 \times 2\ \text{cm}^2$  glass substrate using a smaller mini-well. The two pictures are not to scale.

## 5. Conclusions

Three methods for the reliable deposition of  $^{6}\text{LiF}$  in the form of thin layers on various types of substrates have been described, to be used as neutron converters on top of semi-conductors or kinds of detectors. Two methods exploit the physical vapor deposition in a smaller and a larger evaporator, respectively, for limited or more considerable production. The third one is a fast and simplified chemical process suitable for the production of a single unit or a few units. Each method has its own benefits and limitations, and their availability represents a versatile set of tools that covers a wide spectrum of possible future needs for this type of neutron converter.

**Author Contributions:** Conceptualization and supervision P.F. and L.C.; design P.F., L.C., F.L., C.M. and A.M.; construction C.M., A.M. and M.U.; test and measurements A.M., M.U., F.L., L.C., G.E.P. and P.F.; simulations S.A.; manuscript preparation P.F. All authors have read and agreed to the published version of the manuscript.

**Funding:** Part of this work was funded within the framework of: (i) European Union’s Horizon 2020 research and innovation program under grant agreement No. 847641, project MICADO (Measurement and Instrumentation for Cleaning And Decommissioning Operations); (ii) European Union’s Horizon 2020 research and innovation program under grant agreement No. 945335, Project CLEANDEM (Cyber physical Equipment for unManned Nuclear DEcommissioning Measurements).

**Data Availability Statement:** The data presented in this study are available on request from the corresponding author.

**Conflicts of Interest:** The authors declare no conflict of interest.

## References

1. Kouzes, R.T.; Siciliano, E.R.; Ely, J.H.; Keller, P.E.; McConn, R.J. Passive neutron detection at borders. In Proceedings of the 2007 IEEE Nuclear Science Symposium Conference Record, Honolulu, HI, USA, 26 October–3 November 2007; Volume 2, p. 1115.
2. Ovechkina, L.; Riley, K.; Miller, S.; Bell, Z.; Nagarkar, V. Gadolinium loaded plastic scintillators for high efficiency neutron detection. *Phys. Proc.* **2009**, *2*, 161–170. [CrossRef]
3. van Loef, E.V.; Glodo, J.; Shirwadkar, U.; Zaitseva, N.; Shah, K.S. Novel organic scintillators for neutron detection. In Proceedings of the 2010 IEEE Nuclear Science Symposium Conference Record (NSS/MIC 2010), Knoxville, TN, USA, 30 October–6 November 2010; pp. 1007–1009.
4. Bell, Z.W.; Miller, M.A.; Maya, L.; Brown, G.M.; Sloop, F.V. Boron-loaded silicone rubber scintillators. *IEEE Trans. Nucl. Sci.* **2004**, *51*, 1773–1776. [CrossRef]
5. Duxbury, D.M.; Rhodes, N.J.; Schooneveld, E.M.; Spill, E.J.; Webster, J.R. Sprinter: A new detector system for the INTER neutron reflectometer. *IEEE Trans. Nucl. Sci.* **2013**, *60*, 1327–1331. [CrossRef]
6. Kouzes, R. *Technical Report PNNL-18388*; Pacific Northwest National Laboratory: Richland, WA, USA, 2009.
7. Kouzes, R.T.; Ely, J.H.; Erikson, L.E.; Kernan, W.J.; Lintreuer, A.T.; Siciliano, E.R.; Stephens, D.L.; Stromswold, D.C.; van Ginhoven, R.M.; Woodring, M.L. Neutron detection alternatives to  $^3\text{He}$  for national security applications. *Nucl. Instrum. Methods Phys. Res. A* **2010**, *623*, 1035–1045. [CrossRef]
8. Colonna, N.; Pietropaolo, A.; Sacchetti, F.  $^3\text{He}$  replacement in neutron detection: Current status and perspectives. *Eur. Phys. J. Plus* **2015**, *130*, 236. [CrossRef]
9. Henzlova, D.; Kouzes, R.; McElroy, R.; Peerani, P.; Aspinall, M.; Baird, K.; Bakel, A.; Borella, M.; Bourne, M.; Bourva, L.; et al. Current Status of  $^3\text{He}$  Alternative Technologies for Nuclear Safeguards. NNSA USDOE and EURATOM, LA-UR-15-21201. Available online: <https://www.osti.gov/biblio/1227248> (accessed on 19 October 2022).
10. Barbagallo, M.; Cosentino, L.; Forcina, V.; Marchetta, C.; Pappalardo, A.; Peerani, P.; Scirè, C.; Scirè, S.; Schillaci, M.; Vaccaro, S.; et al. Thermal neutron detection using a silicon pad detector and  $^6\text{LiF}$  removable converters. *Rev. Sci. Instrum.* **2013**, *84*, 033503. [CrossRef] [PubMed]
11. McGregor, D.S.; Hammig, M.D.; Yang, Y.H.; Gersch, H.K.; Klann, R.T. Design consideration for thin film coated semiconductor thermal neutron detectors—I: Basics regarding alpha particle emitting neutron reactive films. *Nucl. Instr. Meth. Phys. Res. A* **2003**, *500*, 272–308. [CrossRef]
12. Baker, C.; Green, K.; van der Grinten, M.; Iaydjiev, P.; Ivanov, S.; Al-Ayoubi, S.; Harris, P.; Pendlebury, J.; Shiers, D.; Geltenbort, P. Development of solid-state silicon devices as ultra cold neutron detectors. *Nucl. Instr. Meth. Phys. Res. A* **2002**, *487*, 511–520. [CrossRef]
13. Philips, B.F.; Kub, F.J.; Novikova, E.I.; Wulf, E.A.; Fitzgerald, C. Neutron detection using large area silicon detectors. *Nucl. Instr. Meth. Phys. Res. A* **2007**, *579*, 173–176. [CrossRef]
14. Uher, J.; Fröjd, C.; Jakúbek, J.; Kenney, C.; Kohout, Z.; Linhart, V.; Parker, S.; Petersson, S.; Pospíšil, S.; Thungström, G. Characterization of 3D thermal neutron semiconductor detectors. *Nucl. Instr. Meth. Phys. Res. A* **2007**, *576*, 32–37. [CrossRef]
15. Voytchev, M.; Iñiguez, M.P.; Méndez, R.; Mañanes, A.; Rodríguez, L.R.; Barquero, R. Neutron detection with a silicon PIN photodiode and  $^6\text{LiF}$  converter. *Nucl. Instr. Meth. Phys. Res. A* **2003**, *512*, 546–552. [CrossRef]
16. Pappalardo, A.; Barbagallo, M.; Cosentino, L.; Marchetta, C.; Musumarra, A.; Scirè, C.; Scirè, S.; Vecchio, G.; Finocchiaro, P. Characterization of the silicon +  $^6\text{LiF}$  thermal neutron detection technique. *Nucl. Instr. Meth. Phys. Res. A* **2016**, *810*, 6–13. [CrossRef]
17. Finocchiaro, P.; Cosentino, L.; Lo Meo, S.; Nolte, R.; Radeck, D. Absolute efficiency calibration of  $^6\text{LiF}$ -based solid state thermal neutron detectors. *Nucl. Instr. Meth. Phys. Res. A* **2018**, *885*, 86–90. [CrossRef]
18. Cosentino, L.; Musumarra, A.; Barbagallo, M.; Colonna, N.; Damone, L.; Pappalardo, A.; Piscopo, M.; Finocchiaro, P. Silicon detectors for monitoring neutron beams in n-TOF beamlines. *Rev. Sci. Instrum.* **2015**, *86*, 073509. [CrossRef] [PubMed]
19. Pappalardo, A.; Vasi, C.; Finocchiaro, P. Direct comparison between solid state Silicon+ $^6\text{LiF}$  and  $^3\text{He}$  gas tube neutron detectors. *Results Phys.* **2016**, *6*, 12–13. [CrossRef]
20. Cosentino, L.; Ducasse, Q.; Giuffrida, M.; Lo Meo, S.; Longhitano, F.; Marchetta, C.; Massara, A.; Pappalardo, P.; Passaro, G.; Russo, S.; et al. SiLiF Neutron Counters to Monitor Nuclear Materials in the MICADO Project. *Sensors* **2021**, *21*, 2630. [CrossRef]
21. MICADO Project. Available online: <https://www.micado-project.eu/> (accessed on 19 October 2022).
22. CLEANDEM Project. Available online: <https://cordis.europa.eu/project/id/945335/> (accessed on 19 October 2022).

23. Sigma Aldrich. Available online: <https://www.sigmaaldrich.com/> (accessed on 19 October 2022).
24. Finocchiaro, P. Eloss\_and\_Bragg\_v219.xlsb worksheet. unpublished.

**Disclaimer/Publisher's Note:** The statements, opinions and data contained in all publications are solely those of the individual author(s) and contributor(s) and not of MDPI and/or the editor(s). MDPI and/or the editor(s) disclaim responsibility for any injury to people or property resulting from any ideas, methods, instructions or products referred to in the content.